



This is a repository copy of *Fully-integrated transformer with asymmetric primary and secondary leakage inductances for a bidirectional resonant converter*.

White Rose Research Online URL for this paper:

<https://eprints.whiterose.ac.uk/196917/>

Version: Accepted Version

Article:

Arab Ansari, S. orcid.org/0000-0003-2293-0009, Davidson, J.N. and Foster, M.P. (2023) Fully-integrated transformer with asymmetric primary and secondary leakage inductances for a bidirectional resonant converter. *IEEE Transactions on Industry Applications*, 59 (3). pp. 3674-3685. ISSN 0093-9994

<https://doi.org/10.1109/TIA.2023.3252525>

© 2023 The Authors. Except as otherwise noted, this author-accepted version of a journal article published in *IEEE Transactions on Industry Applications* is made available via the University of Sheffield Research Publications and Copyright Policy under the terms of the Creative Commons Attribution 4.0 International License (CC-BY 4.0), which permits unrestricted use, distribution and reproduction in any medium, provided the original work is properly cited. To view a copy of this licence, visit <http://creativecommons.org/licenses/by/4.0/>

Reuse

This article is distributed under the terms of the Creative Commons Attribution (CC BY) licence. This licence allows you to distribute, remix, tweak, and build upon the work, even commercially, as long as you credit the authors for the original work. More information and the full terms of the licence here: <https://creativecommons.org/licenses/>

Takedown

If you consider content in White Rose Research Online to be in breach of UK law, please notify us by emailing eprints@whiterose.ac.uk including the URL of the record and the reason for the withdrawal request.



eprints@whiterose.ac.uk
<https://eprints.whiterose.ac.uk/>

Fully-integrated Transformer with Asymmetric Primary and Secondary Leakage Inductances for a Bidirectional Resonant Converter

Sajad A. Ansari, Jonathan N. Davidson, and Martin P. Foster

Abstract—Typically, inserted-shunt integrated transformers have symmetric primary and secondary leakage inductances. However, bidirectional resonant converters typically operate more efficiently with different primary and secondary series inductances. In this paper, a new topology for an inserted-shunt integrated transformer which can provide tunable, asymmetric leakage (series) inductances on the primary and secondary sides is presented. Two magnetic shunts, with appropriate air gaps, are inserted between two E-cores and the primary and secondary windings are separated by being placed at opposite sides of the shunts. The proposed transformer is analysed in detail and modelling and design guidelines are provided. It is shown that the magnetising inductance and the primary and secondary leakage inductances are decoupled from each other, and they can be determined separately. The design has the advantage of using planar E-cores and magnetically permeable sheets that are commercially available. The theoretical analysis is verified by simulation and experimental results. In addition, to demonstrate the performance of the proposed integrated transformer in practice, an exemplar bidirectional CLLLC resonant converter is designed, constructed and tested using the new integrated transformer.

Index Terms—Asymmetric leakage inductances, bidirectional converter, CLLLC resonant converter, integrated transformer.

I. INTRODUCTION

RAPID growth of residential energy storage systems (ESSs) is outpacing expectations, and these household systems are becoming important assets. For example, electric vehicles (EVs) with vehicle-to-grid (V2G) capability can be used as distributed energy assets to provide power to the utility loads, to reduce grid frequency fluctuations and to absorb excess energy produced by renewable energy sources [1-3].

A bidirectional dc-dc converter and a bidirectional dc-ac converter are usually used in ESSs to transfer power in both directions between the grid and the batteries. Bidirectional dc-

dc converters likewise manage the power flow between the dc bus and the batteries. The main focus of these dc-dc converters is on achieving low cost, high efficiency and power density, and wide input and output voltage ranges [4, 5].

Pulse-width-modulated (PWM) dc-dc converters, such as the boost converter, suffer from high switching losses due to their hard switching and hence cannot be used at high switching frequencies. The resulting low-frequency designs typically have low power density. Soft-switching capability can usually be achieved for PWM converters by adding an auxiliary circuit to the conventional topology. However, this auxiliary circuit makes the converter more complicated and expensive and provides soft-switching capability for only a narrow range of loads [6, 7].

Resonant converters can provide high efficiency and power density at a low cost since they benefit from soft-switching capability and magnetic integration. Therefore, resonant converters are becoming desirable for dc-dc applications like ESSs [8-10].

The LLC resonant converter is one of the most popular resonant topologies since it can provide high efficiency at high switching frequency and can be designed to obtain high voltage gain at a narrow range of operating frequencies. However, the LLC converter is not suitable for bidirectional power transfer since the shunt inductance is effectively connected in parallel with the chopped battery voltage in regeneration (reverse-direction) mode (RM) meaning that it does not play a role in the resonant tank. The result is that, in RM, an LLC converter is equivalent to a series resonant converter, which is not a suitable converter for wide input and output voltage range applications [11-13].

To adopt the LLC converter for bidirectional power transfer, a bidirectional CLLLC converter, which has an extra capacitor and an extra inductor on the secondary side, is proposed in [14]. The bidirectional CLLLC resonant converter is shown in Fig. 1(a). In [14], the resonant components on the primary and secondary sides of the transformer must be symmetric ($L_{r1} = n^2 L_{r2}$, $C_{r2} = n^2 C_{r1}$, $n = N_p/N_s$) and the converter has unity gain. Unfortunately, the unity gain means the topology is not suitable for applications in which the input and output voltages

S. A. Ansari, J. N. Davidson and M. P. Foster are with the Department of Electronic and Electrical Engineering, University of Sheffield, Sheffield, S1 3JD, United Kingdom (e-mail: sarabansari1@sheffield.ac.uk; jonathan.davidson@sheffield.ac.uk; m.p.foster@sheffield.ac.uk). This work was supported by the Engineering and Physical Sciences Research Council (EPSRC) under grant EP/S031421/1. For the purpose of open access, the authors have applied a creative commons attribution (CC-BY) licence to any author accepted manuscript version arising.

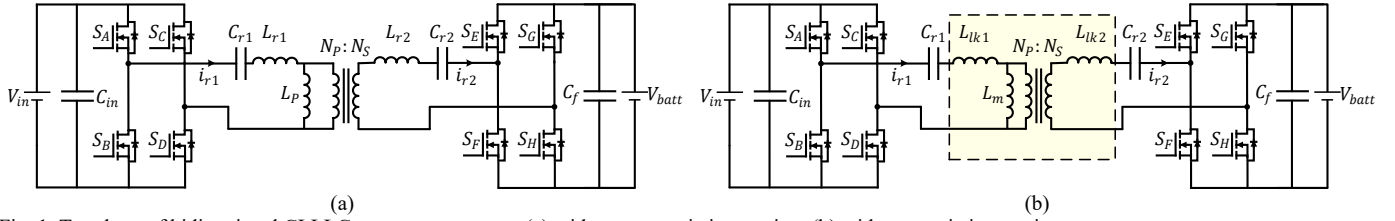


Fig. 1. Topology of bidirectional CLLLC resonant converter, (a) without magnetic integration, (b) with magnetic integration.

vary during power transfer. This is particularly challenging with battery-charging type applications where the specified output voltage often has a wider range (for example, from 250 V to 450 V in vehicle-to-grid (V2G) applications) [15, 16].

In [15, 16], a design methodology for a CLLLC resonant converter is presented so that the converter can operate with wide battery voltage regulation. The converter proposed in [15, 16] is, like [14], based on the LLC topology with an extra inductor and extra capacitor on the secondary side but this time the component values can be asymmetric ($L_{r1} \neq n^2 L_{r2}$ and $C_{r2} \neq n^2 C_{r1}$). In [16], the benefits of asymmetric parameters are discussed in detail and they are again summarised in Fig. 2. Fig. 2 shows the gain plots, in charging and discharging mode, of the CLLLC converter in [16]. For a given operating frequency range, the range of available gains with symmetric and asymmetric primary and secondary inductances and capacitances are shown. The operating frequency range needed for a desired range of gains is significantly smaller for the asymmetric design, allowing optimization to achieve high efficiency, reduced current stress and reduced electromagnetic interference.

The CLLLC resonant converter with asymmetric resonant components not only provides the advantages of the LLC converter but also can provide bidirectional power transfer. The CLLLC converter presented in [15, 16] is therefore a good candidate for battery charging applications and this topology is used in this paper.

The topology of CLLLC converter is shown in Fig. 1(a). Even though this converter benefits from soft switching capability and can be switched at high frequencies, it needs four magnetic components including two series inductors (L_{r1} and L_{r2}), a parallel inductor (L_p) and a transformer, leading to large size and high cost. To increase the efficiency and power density, and to decrease the cost of this converter, these magnetic components can be integrated into a single transformer, as shown in Fig. 1(b).

Magnetic integration has been an important topic in recent years and hence many methods have been proposed in the literature [17-21]. Amongst them, the inserted-shunt integrated planar transformer is well-known because of its many advantages, viz precise estimation of leakage inductance during design, capability for achieving high leakage inductance, the ability to use cores readily available in the market and simple manufacturing [21-24]. A magnetically permeable shunt is inserted between two E-cores with the primary and secondary windings being separated on opposite sides of the shunt. The planar E-cores, which have their own advantages such as high

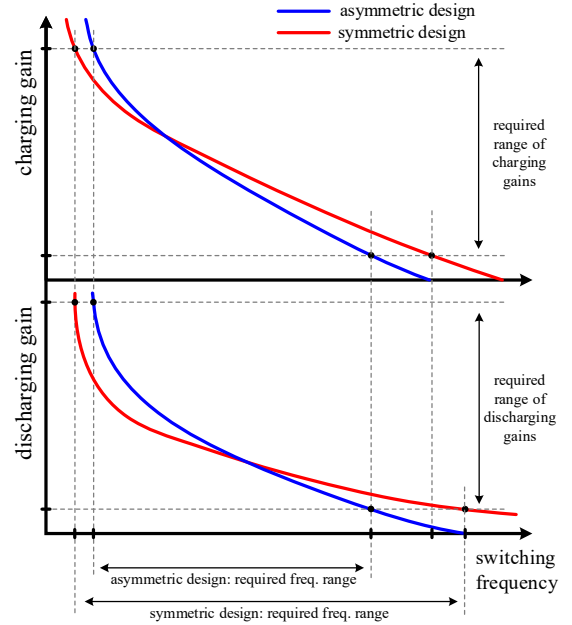


Fig. 2. Comparison of gain for symmetric and asymmetric designs, using data from [16].

power density, improved cooling capability, modularity and manufacturing simplicity, are used for the proposed transformer.

The inserted-shunt integrated transformers discussed above have symmetric primary and secondary leakage inductances and these inductances cannot be designed separately in these transformers. The CLLLC converter presented in [15, 16], and other similar topologies that need asymmetric primary and secondary resonant inductances could address more application challenges (especially the ones that require higher power density) if an integrated magnetic transformer were developed that can provide non-identical (asymmetric) primary and secondary leakage inductances. Therefore, a new design methodology for the inserted-shunt integrated transformers is needed that takes into account the non-identical primary and secondary leakage inductances.

In this paper, a new topology for the inserted-shunt integrated magnetic planar transformer is proposed that can provide non-identical primary and secondary leakage inductances. The structure of the proposed integrated transformer is shown in Fig. 3. Two magnetic shunts are inserted between two E-cores and the primary and secondary windings are separated by being placed at different sides of the magnetic shunts. Commercially available planar cores can be

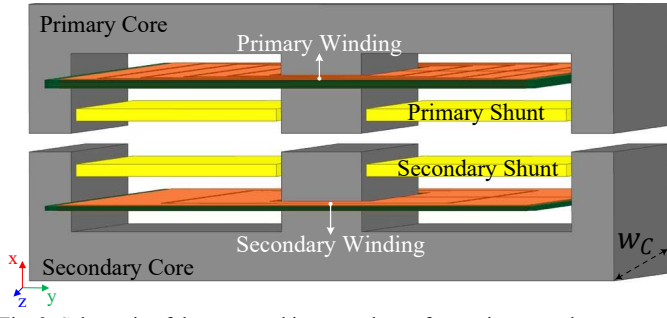


Fig. 3. Schematic of the proposed integrated transformer in x-y-z plane.

used for the E-cores and magnetic (ferrite) sheets, which are again commercially available, can be used for the shunts, leading to cheaper and easier manufacturing.

The proposed integrated transformer is analysed in detail and its modelling and design guidelines are provided. It is shown that the magnetising inductance and the primary and secondary leakage inductances are decoupled, and they can be determined separately in the proposed topology. This theoretical analysis is verified by simulation and experimental results. To investigate performance, an exemplar CLLC converter is designed using the proposed integrated transformer to provide experimental validation of the design process. It is shown that the implemented bidirectional CLLC resonant converter operates properly while all its magnetic components are integrated into the proposed transformer.

This study builds on preliminary results [25] presented at the 11th International Conference on Power Electronics, Machines and Drives, 2022, by including a more complete literature review, further theoretical analysis and experimental validation.

The paper is organised as follows: the proposed integrated transformer is fully described and then modelled in Section II. In Section III, the calculation of the primary and secondary leakage inductances is investigated. The presented modelling is discussed in Section IV and verified by finite element analysis (FEA) in Section V. In Section VI, experimental verification is presented. A brief conclusion to the work is provided in Section VII.

II. PROPOSED INSERTED-SHUNT INTEGRATED TRANSFORMER

The schematic of the proposed integrated transformer is shown in Fig. 3. The structure is divided into primary and secondary sections. The primary section contains an E-core (primary core), a magnetic shunt (primary shunt) and a winding (primary winding), and the secondary section contains the corresponding secondary pieces (secondary core, the shunt and winding). With reference to the equivalent circuit shown in Fig. 4, the operating principle of the transformer is summarised below with more detailed descriptions being provided in the following sections.

The primary winding generates a flux in the primary core and this is responsible for producing the primary side inductance (L_{PP} in Fig. 4(a)) of which the magnetising inductance (L_m in Fig. 4(b)) is the largest contributor. A small

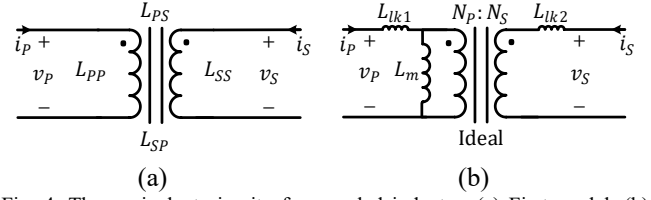


Fig. 4. The equivalent circuit of a coupled inductor. (a) First model. (b) Second model.

but significant proportion of the primary flux flows through the primary shunts and is responsible for the primary side leakage inductance, L_{1k1} . Similar arguments lead to the provision of the secondary side leakage inductance (L_{1k2}). The remaining primary flux crosses the air-gap and couples to the secondary winding and so is responsible for the ideal transformer $N_P:N_S$ in Fig. 4(b).

A. Basic definition of magnetising and primary and secondary leakage inductances

The equivalent circuit of a coupled inductor is shown in Fig. 4(a). This equivalent circuit can be expressed as (1) [20, 26].

$$\begin{bmatrix} v_P \\ v_S \end{bmatrix} = \begin{bmatrix} L_{PP} & L_{PS} \\ L_{SP} & L_{SS} \end{bmatrix} \frac{d}{dt} \begin{bmatrix} i_P \\ i_S \end{bmatrix} \quad (1)$$

where L_{PP} and L_{SS} are primary and secondary self-inductances, respectively, L_{PS} and L_{SP} are mutual inductances and i_P and i_S are the primary and secondary currents, respectively.

The coupled inductor can also be represented by the three-inductor model shown in Fig. 4(b). This equivalent circuit can be expressed as (2). In (2), N_P and N_S are the number of primary and secondary turns, respectively, L_{1k1} and L_{1k2} are primary and secondary leakage inductances, respectively and L_m is magnetising inductance which may be obtained as shown in (3).

$$\begin{bmatrix} v_P \\ v_S \end{bmatrix} = \begin{bmatrix} L_{1k1} + L_m & \frac{N_S}{N_P} L_m \\ \frac{N_S}{N_P} L_m & L_{1k2} + \frac{N_S^2}{N_P^2} L_m \end{bmatrix} \frac{d}{dt} \begin{bmatrix} i_P \\ i_S \end{bmatrix} \quad (2)$$

$$L_m = \frac{N_P}{N_S} L_{PS} \quad (3)$$

To calculate the magnetising inductance, the mutual inductance, L_{PS} , needs to be obtained. L_{PS} may be obtained as

$$L_{PS} = \frac{N_S}{i_P} \phi_{PS} \quad (4)$$

where ϕ_{PS} is the mutual flux generated by the primary winding. By substituting (4) into (3), the magnetising inductance can be obtained as follows

$$L_m = \frac{N_P}{i_P} \phi_{PS} \quad (5)$$

The primary self-inductance may be obtained from (6), where \mathcal{R} is the total core reluctance experienced by the primary winding (including the air gaps).

$$L_{PP} = \frac{N_P^2}{\mathcal{R}} \quad (6)$$

The primary, L_{1k1} , and secondary, L_{1k2} , leakage inductances can be obtained as (7) and (8), respectively [20, 26].

$$L_{1k1} = L_{PP} - L_m \quad (7)$$

$$L_{1k2} = L_{SS} - \frac{N_S^2}{N_P^2} L_m \quad (8)$$

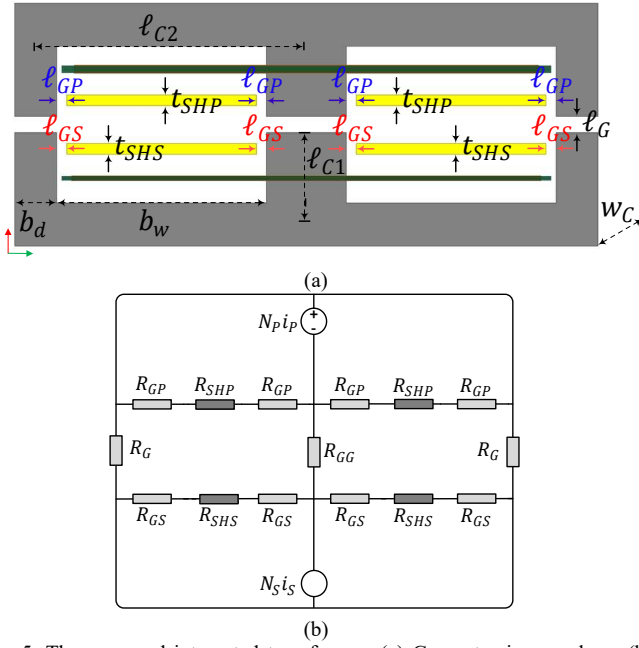


Fig. 5. The proposed integrated transformer. (a) Geometry in x-y plane. (b) Reluctance model.

B. Calculation of magnetising inductance

The structure of the proposed transformer, with its geometry and dimensions, is shown in Fig. 5(a). An air gap of length ℓ_G is inserted between the two E-cores to regulate the magnetising inductance. Air gap ℓ_{GP} is located between primary shunt and primary E-core to set the primary leakage inductance, and air gap ℓ_{GS} is located between secondary shunt and secondary E-core to set the secondary leakage inductance. Fig. 5(b) shows the reluctance model of the proposed integrated transformer. In this model, the permeability of the core is assumed to be much larger than the permeability of the air and the shunts, and thus only the reluctances of the air gaps and shunts are considered for the analysis. In Fig. 5(b), \mathcal{R}_{SHP} and \mathcal{R}_{SHS} are the reluctances of the primary and secondary shunts, respectively; \mathcal{R}_{GP} and \mathcal{R}_{GS} are the air-gap reluctances of the primary and secondary shunts; and \mathcal{R}_G and \mathcal{R}_{GG} are the reluctances of the air gaps between the two E-cores. These reluctances may be obtained as follows:—

$$\mathcal{R}_{SHP} = \frac{b_w - 2\ell_{GP}}{\mu_0 \mu_{SHP} t_{SHP} w_C} \quad (9)$$

$$\mathcal{R}_{SHS} = \frac{b_w - 2\ell_{GS}}{\mu_0 \mu_{SHS} t_{SHS} w_C} \quad (10)$$

$$\mathcal{R}_{GP} = \frac{\ell_{GP}}{\mu_0 (t_{SHP} + \ell_{GP}) (w_C + \ell_{GP})} \quad (11)$$

$$\mathcal{R}_{GS} = \frac{\ell_{GS}}{\mu_0 (t_{SHS} + \ell_{GS}) (w_C + \ell_{GS})} \quad (12)$$

$$\mathcal{R}_G = \frac{\ell_G}{\mu_0 (b_d + \ell_G) (w_C + \ell_G)} \quad (13)$$

$$\mathcal{R}_{GG} = \frac{\ell_G}{\mu_0 (2b_d + \ell_G) (w_C + \ell_G)} \quad (14)$$

where μ_0 is the air permeability and μ_{SHP} and μ_{SHS} are the relative permeabilities of the primary and secondary shunts, respectively. The meaning of other quantities, such as areas, can be found in Fig. 5(a). Hurley, *et al.*, [27] show that the effective cross-sectional area of the air gap with dimensions a by b is

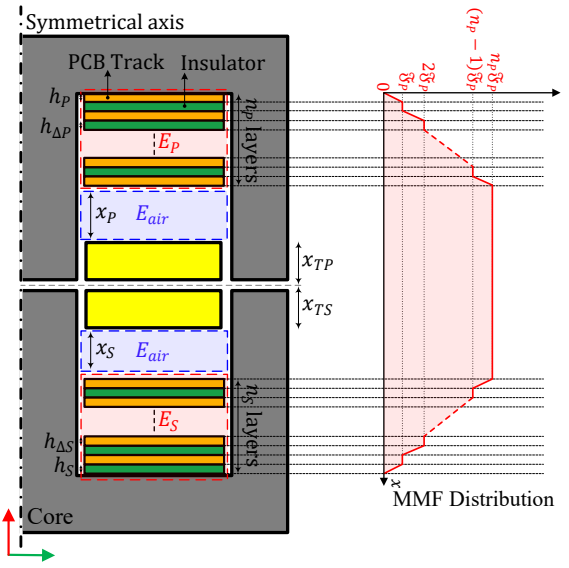


Fig. 6. Right-hand-side cross section showing the energy allocation and associated MMF distribution for the proposed topology.

equal to $(a+g)$ by $(b+g)$ when the fringing effect is considered and g is the length of the studied air-gap.

According to the reluctance model presented in Fig. 5(b), the mutual fluxes ϕ_{PS} and ϕ_{SP} may be approximated by (15) and (16), respectively.

$$\phi_{PS} = \frac{2N_p i_p}{\mathcal{R}_G + 2\mathcal{R}_{GG}} \quad (15)$$

$$\phi_{SP} = \frac{2N_s i_s}{\mathcal{R}_G + 2\mathcal{R}_{GG}} \quad (16)$$

Finally, from (15) and (5), the magnetising inductance may be obtained,

$$L_m = \frac{2N_p^2}{\mathcal{R}_G + 2\mathcal{R}_{GG}} \quad (17)$$

C. Energy stored by primary and secondary leakage inductances

Assuming the permeability of the core is high then any energy that is stored in the transformer must be located outside the core and, therefore, within the window area. Equation (18) shows the total energy stored in the volume of the windings, window area and shunts (including their air gaps, ℓ_{GP} and ℓ_{GS}) is equal to the energy stored in the primary and secondary leakage inductances.

$$E = \frac{1}{2} \iiint_V BH \, dV = \frac{1}{2} L_{lk1} i_p^2 + \frac{1}{2} L_{lk2} i_s^2 \quad (18)$$

where V is the total volume of window area, B is the flux density and H is the magnetic field intensity.

A cross section of the right-hand side of the proposed integrated transformer, divided into several regions contributing to the energy stored by the leakage inductances, is shown in Fig. 6. In Fig. 6, N_p and N_s are the number of primary and secondary turns, respectively; n_p and n_s are the number of the primary and secondary winding layers, respectively; and k_p and k_s are number of turns per layer for the primary and secondary windings ($N_p = k_p n_p$ and $N_s = k_s n_s$), respectively. Each primary winding layer has a thickness h_p and its associated insulating layer has thickness $h_{\Delta p}$. Similar symbols

are used for the secondary winding with each layer having a thickness h_S and insulating layer thickness $h_{\Delta S}$. E_P and E_S refer to the energy stored in the primary and secondary windings. E_{air} is the energy stored in that part of the window which is not occupied by the windings or shunts, and this is divided into a primary region of height x_P and a secondary region of height x_S . Hence, the energy stored in each region and the energy stored in the shunts, E_{SH} , (including their air gaps, ℓ_{GP} and ℓ_{GS}) needs to be obtained and the primary and secondary leakage inductances can be then obtained from $E = E_{\text{air}} + E_P + E_S + E_{\text{SH}}$ and (18).

III. CALCULATION OF PRIMARY AND SECONDARY LEAKAGE INDUCTANCES

As discussed at the end of Section II, to calculate the primary and secondary leakage inductances, the energy stored in each region and the energy stored in the shunts need to be obtained.

A. Energy stored in window area – E_{air}

The magnetomotive force (MMF) of each layer of the primary winding, \mathfrak{F}_P , may be obtained from (19).

$$\mathfrak{F}_P = k_P i_P \quad (19)$$

The MMF within the window area, $\mathfrak{F}_{\text{air}}$, is equal to $n_P \mathfrak{F}_P$ and the magnetic field intensity within the air area, H_{air} , may be found from (20).

$$H_{\text{air}} = \frac{n_P \mathfrak{F}_P}{b_w} \quad (20)$$

From (18), the energy stored in the window (excluding the windings and shunts), E_{air} , (shown in Fig. 6) is given by,

$$E_{\text{air}} = \frac{1}{2} \mu_0 w_C b_w \left(\int_{x_{\text{TP}}}^{x_{\text{TP}}+x_P} H_{\text{air}}^2 dx + \int_{-x_{\text{TS}}-x_S}^{-x_{\text{TS}}} H_{\text{air}}^2 dx \right) \quad (21)$$

where w_C is the core depth and x_P and x_S are the distances from the primary and secondary windings to the primary and secondary shunts, respectively, as defined in Fig. 6.

From (19)-(21), E_{air} in both windows (left and right windows of the E-cores) may be found from (22).

$$E_{\text{air}} = \mu_0 w_C \frac{n_P^2 k_P^2 i_P^2}{b_w} (x_P + x_S) \quad (22)$$

B. Energy stored in primary and secondary windings

The MMF distribution of the transformer is presented in Fig. 6 which is obtained based on a method outlined in [24, 28, 29]. According to Fig. 6, the stored energy in the PCB layers of primary and secondary windings can be found. Ouyang, *et al*, [29] derived a closed-form expression for the energy stored in the primary and secondary windings, shown in (23) and (24), respectively.

$$E_P = \frac{1}{6} \mu_0 \frac{w_C}{b_w} k_P^2 [h_{\Delta P} (2n_P^3 - 3n_P^2 + n_P) + 2h_P n_P^3] i_P^2 \quad (23)$$

$$E_S = \frac{1}{6} \mu_0 \frac{w_C}{b_w} k_S^2 [h_{\Delta S} (2n_S^3 - 3n_S^2 + n_S) + 2h_S n_S^3] i_S^2 \quad (24)$$

C. Energy stored in primary and secondary shunts

The energy stored in the inserted shunts and their corresponding air gaps can be obtained from the reluctance

model using the method outlined by Ansari, *et al*, [8, 22, 30]. According to the reluctance model presented in Fig. 5(b), the self-inductance of the primary and secondary windings may be obtained as shown in (25) and (26), respectively.

$$L_{\text{PP}} = \frac{N_P^2 (\mathcal{R}_{\text{SHP}} + 2\mathcal{R}_{\text{GP}} + \mathcal{R}_G + 2\mathcal{R}_{\text{GG}})}{(\mathcal{R}_{\text{SHP}} + 2\mathcal{R}_{\text{GP}})(\mathcal{R}_G + 2\mathcal{R}_{\text{GG}})} \quad (25)$$

$$L_{\text{SS}} = \frac{N_S^2 (\mathcal{R}_{\text{SHS}} + 2\mathcal{R}_{\text{GS}} + \mathcal{R}_G + 2\mathcal{R}_{\text{GG}})}{(\mathcal{R}_{\text{SHS}} + 2\mathcal{R}_{\text{GS}})(\mathcal{R}_G + 2\mathcal{R}_{\text{GG}})} \quad (26)$$

From (7), (8), (17), (25) and (26), the primary and secondary leakage inductances caused by the inserted shunts and their corresponding air gaps may be calculated as shown in (27) and (28), respectively.

$$L_{\text{lk1SH}} = \frac{2N_P^2}{\mathcal{R}_{\text{SHP}} + 2\mathcal{R}_{\text{GP}}} \quad (27)$$

$$L_{\text{lk2SH}} = \frac{2N_S^2}{\mathcal{R}_{\text{SHS}} + 2\mathcal{R}_{\text{GS}}} \quad (28)$$

Finally, from (18), (22)-(24), (27) and (28), the primary and secondary leakage inductances of the proposed inserted-shunt integrated transformer may be obtained as shown in (29) and (30), respectively.

$$L_{\text{lk1}} = L_{\text{lk1SH}} + \mu_0 w_C \frac{N_P^2}{b_w} (x_P + x_S) + \quad (29)$$

$$\frac{1}{3} \mu_0 \frac{w_C}{b_w} k_P^2 [h_{\Delta P} (2n_P^3 - 3n_P^2 + n_P) + 2h_P n_P^3]$$

$$L_{\text{lk2}} = L_{\text{lk2SH}} + \mu_0 w_C \frac{N_S^2}{b_w} (x_P + x_S) + \quad (30)$$

$$\frac{1}{3} \mu_0 \frac{w_C}{b_w} k_S^2 [h_{\Delta S} (2n_S^3 - 3n_S^2 + n_S) + 2h_S n_S^3]$$

In a design process for the proposed transformer, the required primary and secondary leakage inductances and magnetising inductance can be obtained by (17), (29) and (30). Particular values can be selected for a particular design by regulating the air gaps ℓ_G , ℓ_{GP} and ℓ_{GS} , and the shunt thicknesses t_{SHP} and t_{SHS} .

IV. MODELLING DISCUSSION

The calculated primary and secondary leakage inductances and magnetising inductance of the proposed integrated transformer for different thicknesses of the shunts (t_{SHP} and t_{SHS}), transformer air gap (ℓ_G) and shunt-core air gaps (ℓ_{GP} and ℓ_{GS}) are presented in Figs. 7(a)-(f). An E58/11/38-3F36 core was used as reference to determine the main factors of influence on a design. As shown in Figs. 7(a)-(d), the primary leakage inductance is mainly affected by the primary shunt air gap (ℓ_{GP}), primary shunt thickness (t_{SHP}) and relative permeability of the primary shunt (μ_{SHP}). The secondary shunt's characteristics and transformer air gap (ℓ_G) do not have noticeable influence on the primary leakage inductance. The secondary leakage inductance is mainly affected by the secondary shunt's characteristics (ℓ_{GS} , t_{SHS} and μ_{SHS}) and it is not affected by the characteristics of the primary shunt (ℓ_{GP} , t_{SHP} and μ_{SHP}) or the transformer air gap (ℓ_G). Therefore, in the proposed topology, the primary and secondary leakage inductances are decoupled, and they may be controlled separately by regulating their shunt's characteristics.

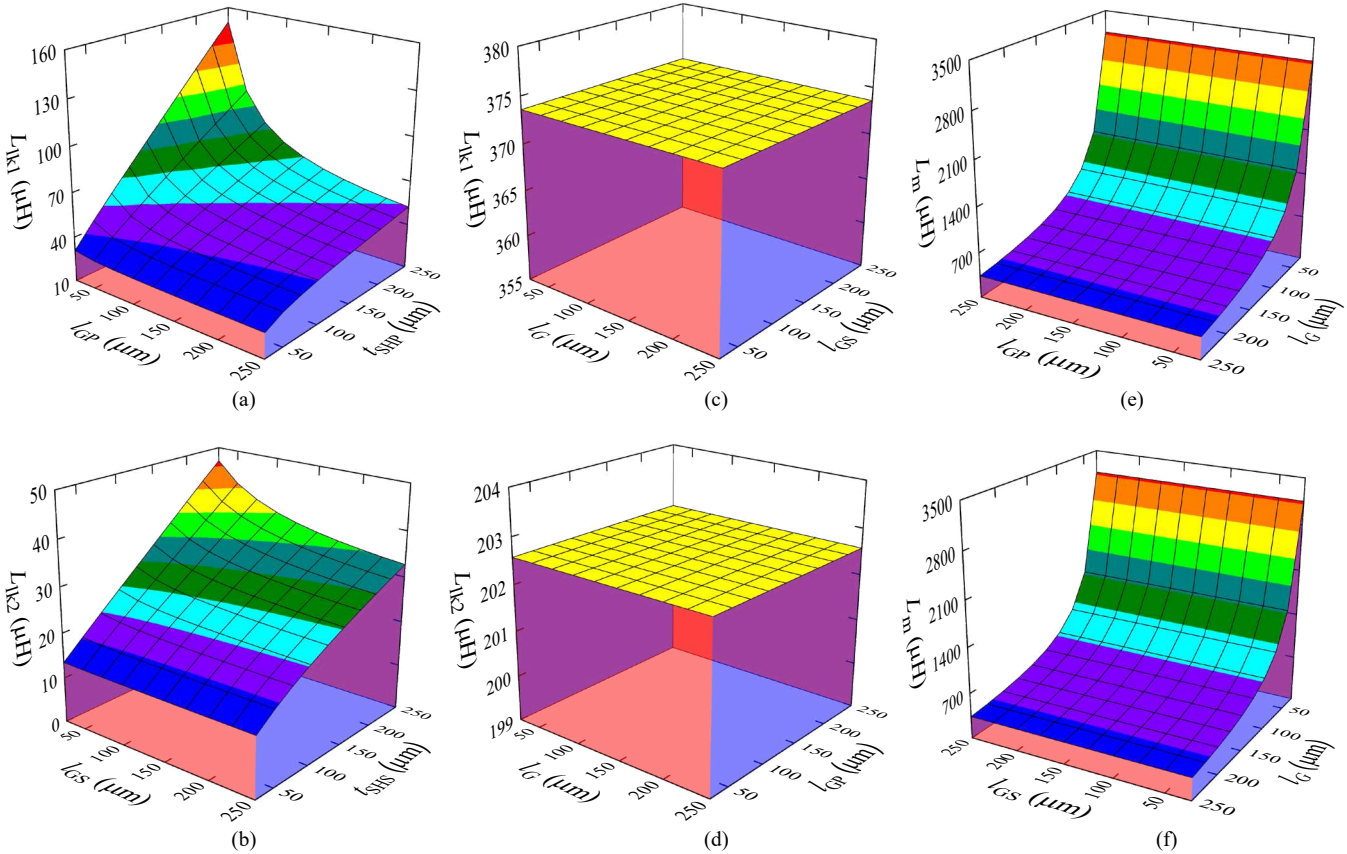


Fig. 7. The calculated leakage and magnetising inductances versus thickness of the shunts, transformer air gap and air gap between the shunts and E-cores. (a) Primary leakage inductance, $t_{SHS}=2\text{mm}$ and $\ell_{GS}=0.1\text{mm}$. (b) Secondary leakage inductance, $t_{SHP}=2\text{mm}$ and $\ell_{GP}=0.1\text{mm}$. (c) Primary leakage inductance, $t_{SHS}=t_{SHP}=2\text{mm}$ and $\ell_{GP}=0.1\text{mm}$. (d) Secondary leakage inductance, $t_{SHS}=t_{SHP}=2\text{mm}$ and $\ell_{GS}=0.1\text{mm}$. (e) Magnetising inductance, $t_{SHS}=t_{SHP}=2\text{mm}$ and $\ell_{GP}=0.1\text{mm}$. (f) Magnetising inductance, $t_{SHS}=t_{SHP}=2\text{mm}$ and $\ell_{GP}=0.1\text{mm}$. Core: E58/11/38-3F36, $\mu_{SHP}=800$, $\mu_{SHS}=100$, $N_P=20$, $N_S=20$, $n_P=5$, $n_S=5$, $k_P=4$, $k_S=4$, $x_P=5\text{mm}$, $x_S=5\text{mm}$.

Figs. 7(e) and (f) show that the magnetising inductance is mainly affected by the transformer air gap, ℓ_G , and does not change appreciably by varying the shunts' air gaps, thicknesses and relative permeabilities (ℓ_{GP} , ℓ_{GS} , t_{SHP} , t_{SHS} , μ_{SHP} and μ_{SHS}). Therefore, in the proposed integrated transformer, the leakage and magnetising inductances are sufficiently decoupled.

The transformer can be designed for most reasonable magnetic component values including the leakage and magnetising inductances. Careful designs can provide different primary and secondary leakage inductances. Because the leakage (series) inductances can be selected independently of each other, a CLLC resonant converter or similar topology which uses the proposed integrated transformer can be designed with high flexibility. In addition, the transformer provides all four (asymmetric) magnetic components.

The proposed topology does not require any unusual core-piece geometries and those widely available commercially can be used. In addition, magnetic (ferrite) sheets, which are available in different sizes and can be cut easily, can be used for the inserted shunts. It should be noted that the proposed inserted-shunt integrated transformer would need an atypical former design for massive production. However, a bespoke

former is already needed for any inserted-shunt integrated transformers.

In addition, where a design requires it, the proposed topology can achieve identical primary and secondary leakage inductances by regulating the primary and secondary shunts air gaps. This compares favourably to conventional inserted-shunt integrated transformers which typically have minor asymmetry due to differences between primary and secondary window areas and winding design in these transformers.

V. SIMULATION RESULTS

To verify the inductance equations provided in Sections II and III, an integrated transformer was simulated using the parameters presented in Table I. The integrated transformer is designed for embedding within a CLLC resonant converter with specifications presented in Table II. The electrical specifications provided in Table II are achieved using the design methodology described in [15] and they are translated into the integrated transformer equivalent circuit components (see Figs. 1(a) and (b)). Following the transformer design process described in the Magnetics Inc design catalogue [31], a suitable core is chosen allowing the minimum number of turns for the primary and secondary windings to be determined. The

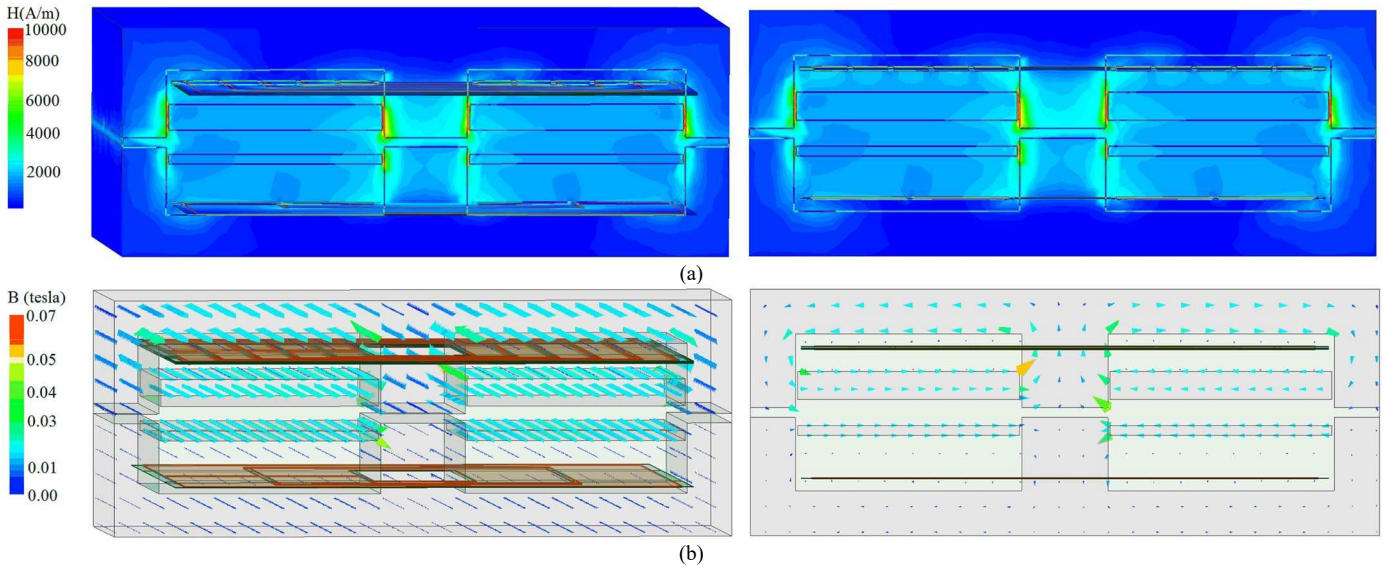


Fig. 8. FEA simulation results. (a) Magnetic field intensity. (b) Magnetic flux density vectors. Frequency=100 kHz.

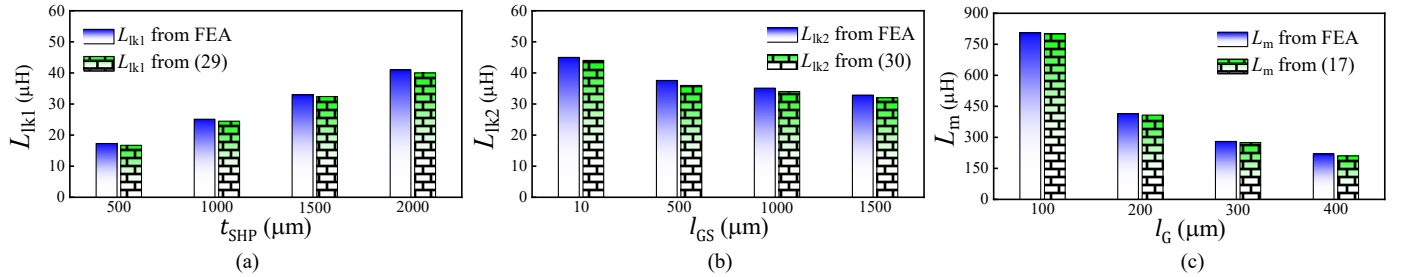


Fig. 9. Modelling validation by FEA. (a) Primary leakage inductance ($l_{GP} = 0.2\text{mm}$). (b) Secondary leakage inductance ($t_{SHS} = 2\text{mm}$). (c) Magnetising inductance. Core: E58/11/38-3F36, $\mu_{SHP} = \mu_{SHS} = 10$, $N_P = 20$, $N_S = 20$, $n_P = 5$, $n_S = 5$, $k_P = 4$, $k_S = 4$, $x_P = 5\text{mm}$, $x_S = 5\text{mm}$.

transformer core (E58/11/38-3F36) is selected based on the power, voltage and frequency suitability guidelines in [31]. The KEMET polymer magnetic shielding sheet (series EFS) is chosen for both the primary and the secondary shunts.

The magnetising inductance, primary and secondary leakage inductances and turns ratio of the designed transformer are chosen to suit the CLLC resonant converter (Table II). The thickness and air-gap length of the primary and secondary shunts (l_{GP} , l_{GS} , t_{SHP} and t_{SHS}) are estimated in order to provide the required primary and secondary leakage

inductances, using (29) and (30), and considering the dimensions of the selected core. Similarly, the transformer air-gap length (l_G) is estimated to provide the required magnetising inductance, using (17).

The designed integrated transformer is simulated in Ansys Maxwell, and the simulation results while the transformer is used in the exemplar CLLC resonant converter are presented in this section.

The magnetic field intensity and flux density vectors for the proposed integrated transformer are shown in Figs. 8(a) and (b), respectively. As shown, the magnetic field intensity and flux density vectors are dominant in the shunts and their air gaps

TABLE I
PROPOSED STRUCTURE'S PARAMETERS

Symbol	Parameter	Value
N_P	Primary turns	20
N_S	Secondary turns	4
k_P	Turns per layer in primary	5
k_S	Turns per layer in secondary	2
n_P	Number of primary layers	4
n_S	Number of secondary layers	2
h_P, h_S	Primary and secondary conduction thickness	55, 70 μm
$h_{\Delta P}, h_{\Delta S}$	Primary and secondary insulation thickness	45, 60 μm
t_{SHP}	Primary shunt thickness	2.5 mm
t_{SHS}	secondary shunt thickness	1.2 mm
l_G	Transformer air gap	0.9 mm
l_{GP}	Distance between primary shunt and E-core	0.2 mm
l_{GS}	Distance between secondary shunt and E-core	0.32 mm
x_P	Distance between primary winding and shunt	3.5 mm
x_S	Dist. between secondary winding and shunt	4.5 mm

TABLE II
THE IMPLEMENTED CLLC CONVERTER'S SPECIFICATION

Symbol	Parameter	Value
$N_P : N_S$	Turns ratio	20:4
L_m	Magnetising inductance	110 μH
L_{r1}	Primary resonant inductance	50 μH
L_{r2}	Secondary resonant inductance	1.2 μH
C_{r1}	Primary resonant capacitance	39 nF
C_{r2}	Secondary resonant capacitance	1 μF
V_{in}	Input voltage	125 V
V_{out}	Output voltage	20-26 V
P_{out}	Output power	200 W
f_s	Switching frequency	60-130 kHz
S_P	Primary switches	IPW65R110CFDA
S_S	Secondary switches	IRFP4137PBF

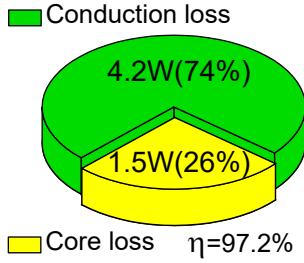


Fig. 10. Loss distribution of the proposed topology for output power of 200W and frequency of 100 kHz.

TABLE III
PARAMETERS OF THE IMPLEMENTED INTEGRATED TRANSFORMER

Parameter	FEA modelling	Simulation	Measurement
Magnetising inductance, L_m	111 μH	113 μH	109 μH
Primary leakage inductance, L_{lk1}	47.9 μH	51.2 μH	49.5 μH
Secondary leakage inductance, L_{lk2}	1.15 μH	1.24 μH	1.20 μH

(ℓ_{GP} and ℓ_{GS}) rather than window region and PCB windings. Therefore, the main part of the energy stored by the leakage inductances is caused by the inserted shunts and their air gaps. In addition, since the magnetic field intensity is highest in the transformer air gap (ℓ_G), the energy stored in the magnetising inductance is mainly stored in ℓ_G .

The primary and secondary leakage inductances and the magnetising inductance versus thickness of the shunts (t_{SHP} and t_{SHS}) and transformer air gap (ℓ_G) obtained from (17), (29) and (30) and measured by FEA simulation are presented in Fig. 9(a)-(c), respectively. As shown, the FEA confirms the proposed model derived in Sections II and III since there is good agreement between the values achieved from the modelling and simulation results.

Loss distribution of the proposed topology is presented in Fig. 10. As shown, the conduction losses are the dominant losses in the proposed topology which are mainly because of AC losses in the winding.

VI. EXPERIMENTAL VERIFICATION

An integrated transformer based on the proposed structure with parameters presented in Table I is built, as shown in Fig. 11. E58/11/38-3F36 is used for the cores and the shunts for this prototype were made by cutting KEMET polymer magnetic shielding sheets (series EFS) and gluing them in parallel to create a stack with the desired thickness.

The measured leakage and magnetising inductances of the constructed transformer, obtained using an Omicron Bode 100 vector network analyser, are presented in Table III. As shown, the primary and secondary leakage inductances and magnetising inductance obtained by modelling are close to the experimental and simulation results. In addition, the proposed structure provides different primary and secondary leakage inductances.

AC resistance, primary and secondary self-inductances,

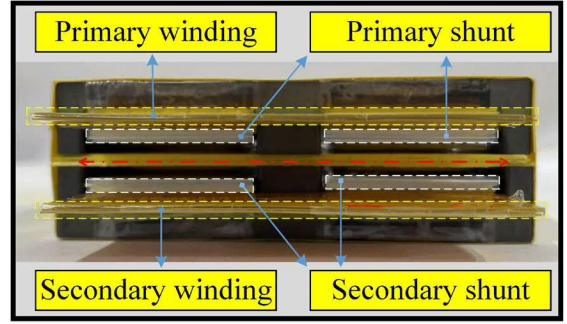


Fig. 11. Prototype implemented transformers.

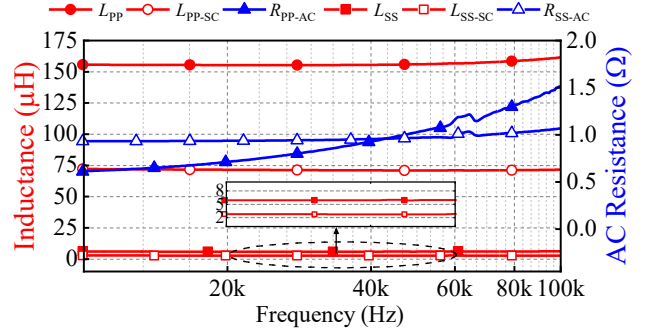


Fig. 12. Primary AC resistance, R_{pp-AC} , secondary AC resistance, R_{ss-AC} , primary self-inductance, L_{pp} , Secondary self-inductance, L_{ss} , primary inductance with secondary shorted, L_{pp-SC} , and secondary inductance with primary shorted, L_{ss-SC} for the proposed integrated transformer.



Fig. 13. Prototype of the implemented CLLLC resonant converter.

measured inductance from the primary winding while the secondary winding is short-circuited, and the measured inductance from the secondary winding while the primary winding is short-circuited versus frequency for the constructed transformer are presented in Fig. 12. As shown, the AC resistance increases with frequency, which is due to high-frequency phenomena including skin and fringing effects. The primary and secondary leakage inductances and magnetising inductance presented in Table III are obtained from data presented in Fig. 12 and the method outlined by Ansari, *et al.*, [32].

To examine the performance of the proposed topology in practice, it was incorporated within an exemplar bidirectional CLLLC resonant converter designed according to the procedure outlined in [15]. The prototype of the converter is shown in Fig. 13 and its specification is presented in Table II in which all four

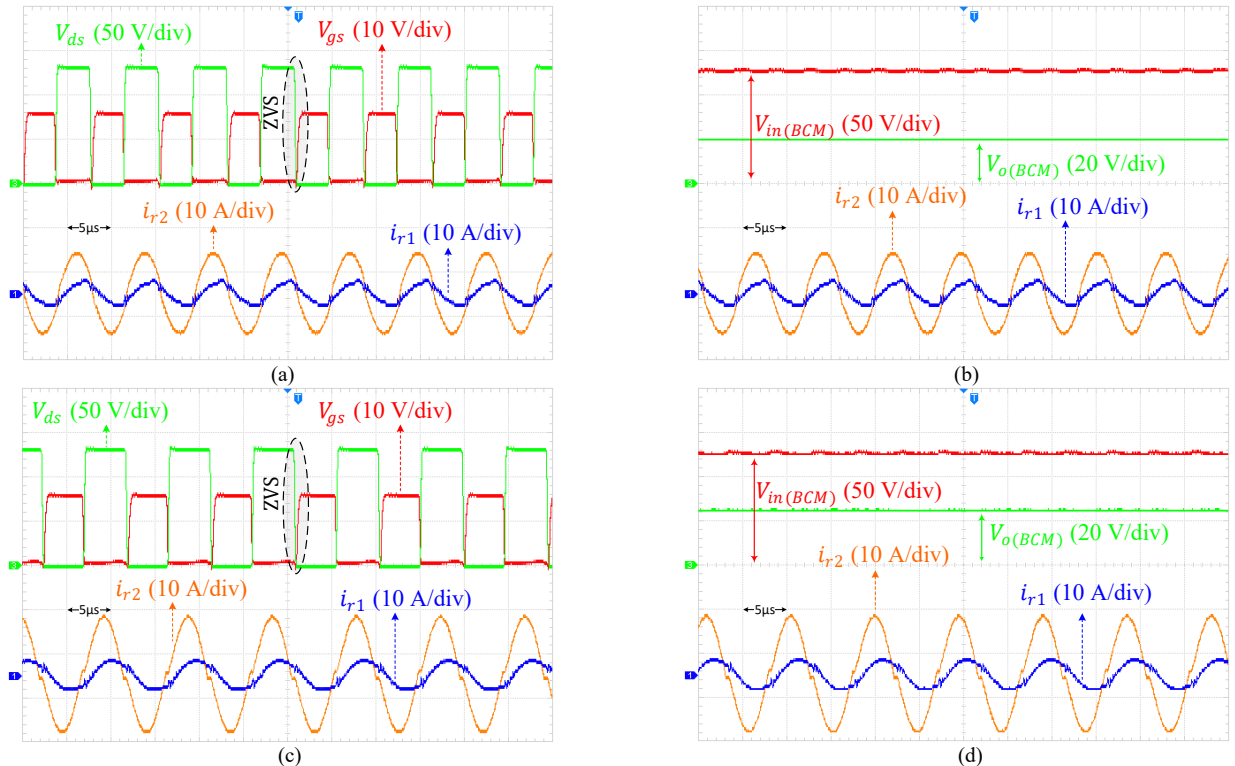


Fig. 14. Experimental waveforms of the CLLC resonant converter in BCM. (a) V_{gs} , V_{ds} , i_{r1} and i_{r2} ($f_s=130$ kHz, $V_{o(BCM)} = 20$ V, $V_{in(BCM)} = 125$ V and $I_{o(BCM)} \cong 7$ A). (b) $V_{o(BCM)}$, $V_{in(BCM)}$, i_{r1} and i_{r2} ($f_s=130$ kHz and $I_{o(BCM)} \cong 7$ A). (c) V_{gs} , V_{ds} , i_{r1} and i_{r2} ($f_s=105$ kHz, $V_{o(BCM)} = 26$ V, $V_{in(BCM)} = 125$ V and $I_{o(BCM)} \cong 9$ A). (d) $V_{o(BCM)}$, $V_{in(BCM)}$, i_{r1} and i_{r2} ($f_s=105$ kHz and $I_{o(BCM)} \cong 9$ A). $I_{o(BCM)}$ is output current in BCM, V_{ds} is drain-to-source voltage, V_{gs} is gate-to-source voltage, i_{r1} and i_{r2} are the primary and secondary resonant currents, respectively (defined in Fig. 1).

series and parallel inductances are integrated into the transformer. As presented in Table II, in battery charging mode (BCM), the exemplar bidirectional converter should be able to provide output voltage (battery voltage, $V_{o(BCM)}$) ranging from 20 V to 26 V while the input voltage (dc bus voltage, $V_{in(BCM)}$) is constant at 125 V. In regeneration mode (RM), the converter must therefore provide a constant voltage of 125 V at its output (dc bus voltage, $V_{o(RM)}$) while the input voltage (battery voltage, $V_{in(RM)}$) varies from 20 V to 26 V.

The waveforms of the CLLC converter switching at 105 kHz and 130 kHz using the proposed topology are presented for BCM in Figs. 14(a)-(d). As shown, the converter operates correctly since the MOSFETs are turned on at zero voltage because the gate-source voltage (of switch S_D , Fig. 1) rises after the drain-source voltage drops to zero while the converter provides 20 V and 26 V at the output.

The waveforms of the CLLC converter operating at 60 kHz and 80 kHz switching frequency using the proposed topology are presented for RM in Figs. 15(a)-(d). As shown, the converter operates correctly since the MOSFETs are turned on at zero voltage because the gate-source voltage (of switch S_H , Fig. 1) rises after its drain-source voltage drops to zero, and the converter provides 125 V at the output while the input voltage varies from 20 V to 26 V.

The efficiency of the CLLC converter at different loads for BCM and RM using the proposed integrated transformer is presented in Fig. 16.

Thermal images of the proposed integrated transformer, while it is used in the implemented CLLC resonant converter for BCM and RM, are shown in Fig. 17(a) and (b), respectively.

As shown, the proposed transformer operates at 37.9°C and 39.8°C for BCM and RM, respectively, and these temperatures do not damage the windings and core. In addition, the temperature of windings is higher than the cores since conduction losses are the dominant loss mode in the proposed inserted-shunt integrated transformer, verifying the loss distribution presented in Fig. 10.

It should be noted that the application of the proposed integrated transformer is not only restricted to the CLLC resonant converter; it can be extended to other similar converters.

VII. CONCLUSION

A topology for an inserted-shunt integrated planar transformer was proposed which can provide different primary and secondary leakage inductances. The proposed topology is suitable for bidirectional converters like the CLLC resonant converter and it can integrate all required magnetic components into a single transformer. The proposed structure can be constructed using cores and magnetic (ferrite) sheets readily available on the market; it does not need bespoke magnetic components. The proposed topology is analysed in detail. It is shown that the magnetising inductance and the primary and secondary leakage inductances are decoupled and can be determined separately. FEA is used to verify the theoretical analysis. A bidirectional CLLC resonant converter is constructed to demonstrate the transformer and investigate its practical performance. The operating waveforms of the converter in both BCM and RM for different switching

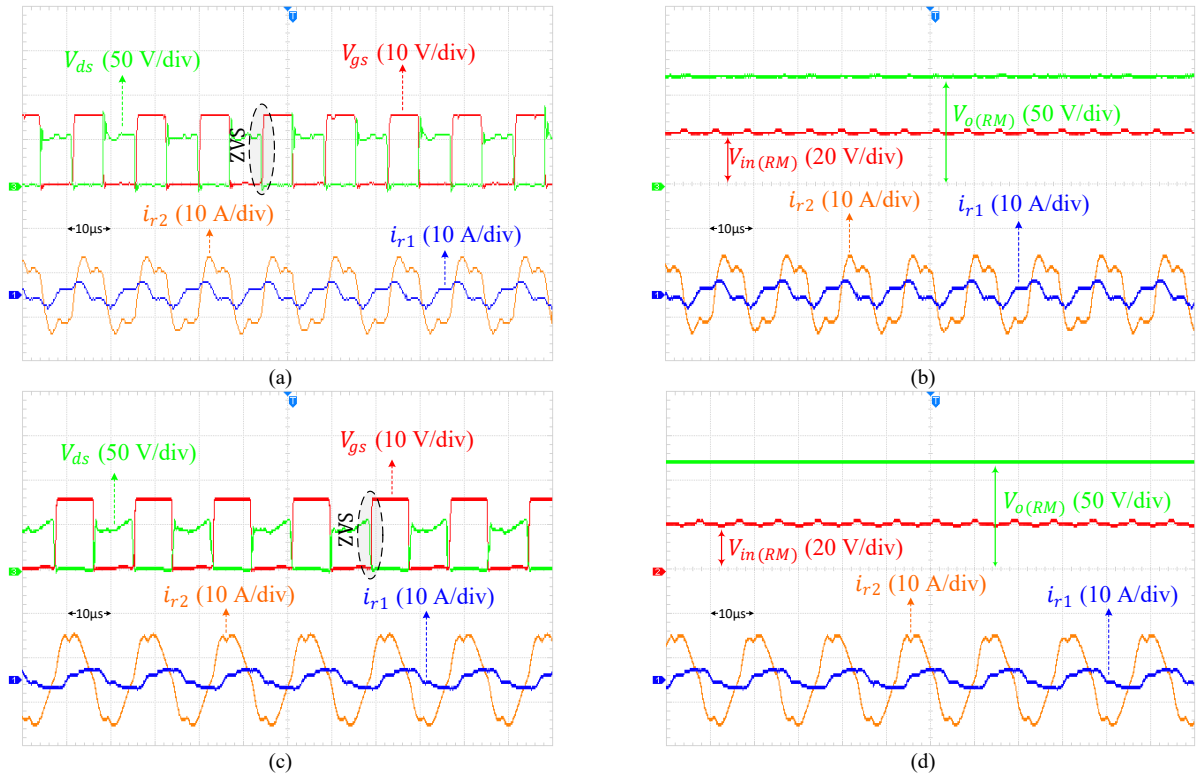


Fig. 15. Experimental waveforms of the CLLC resonant converter in RM. (a) V_{gs} , V_{ds} , i_{r1} and i_{r2} ($f_s=80$ kHz, $V_{o(RM)} = 125$ V, $V_{in(RM)} = 26$ V and $I_{o(RM)} \cong 1.6$ A). (b) $V_{o(RM)}$, $V_{in(RM)}$, i_{r1} and i_{r2} ($f_s=80$ kHz and $I_{o(RM)} \cong 1.6$ A). (c) V_{gs} , V_{ds} , i_{r1} and i_{r2} ($f_s=60$ kHz, $V_{o(RM)} = 125$ V, $V_{in(RM)} = 20$ V and $I_{o(RM)} \cong 1.6$ A). (d) $V_{o(RM)}$, $V_{in(RM)}$, i_{r1} and i_{r2} ($f_s=60$ kHz and $I_{o(RM)} \cong 1.6$ A). $I_{o(RM)}$ is output current in RM.

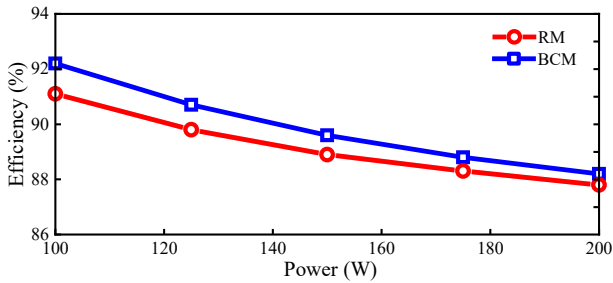


Fig. 16. Efficiency of the CLLC resonant converter for BCM and RM.

frequencies are presented. In addition, thermal images and efficiency measurements for both BCM and RM are presented. Results confirm that the proposed structure can integrate all four magnetic components of an efficient CLLC converter into a single planar transformer.

REFERENCES

[1] Y. Zuo, X. Pan, and C. Wang, "A Reconfigurable Bidirectional isolated LLC Resonant Converter for Ultra-Wide Voltage-gain Range applications," *IEEE Transactions on Industrial Electronics*, vol. 69, no. 6, pp. 5713 - 5723, 2021.

[2] Y. Zhang, D. Zhang, J. Li, and H. Zhu, "Bidirectional LCLL Resonant Converter With Wide Output Voltage Range," *IEEE Transactions on Power Electronics*, vol. 35, no. 11, pp. 11813-11826, 2020.

[3] A. Soni and A. K. Dhakar, "Bi-Directional CLLC Resonant Converter with Integrated Planar Transformer for Energy Storage Systems," in *IECON 2020 The 46th Annual Conference of the IEEE Industrial Electronics Society*, 2020: IEEE, pp. 4255-4260.

[4] X. Ma, P. Wang, H. Bi, and Z. Wang, "A Bidirectional LLCL Resonant DC-DC Converter With Reduced Resonant Tank Currents

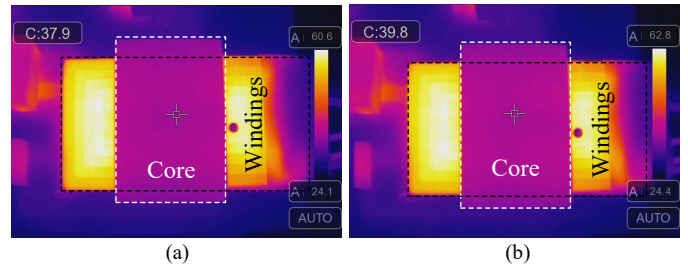


Fig. 17. Thermal images of the transformer for (a) BCM and (b) RM.

and Reduced Voltage Stress of the Resonant Capacitor," *IEEE Access*, vol. 8, pp. 125549-125564, 2020.

[5] M. Mohammadi, A. Dehbashi, G. B. Gharehpetian, A. Khoshsaadat, and P. Mattavelli, "A Family of Soft-Switching DC-DC Converters With Two Degrees of Freedom," *IEEE Transactions on Industrial Electronics*, vol. 68, no. 10, pp. 9398-9409, 2020.

[6] S. A. Ansari, J. N. Davidson, and M. P. Foster, "Evaluation of silicon MOSFETs and GaN HEMTs in soft-switched and hard-switched DC-DC boost converters for domestic PV applications," *IET Power Electronics*, vol. 14, no. 5, pp. 1032-1043, 2021.

[7] S. A. Ansari and J. S. Moghani, "A novel high voltage gain noncoupled inductor SEPIC converter," *IEEE Transactions on Industrial Electronics*, vol. 66, no. 9, pp. 7099-7108, 2018.

[8] S. A. Ansari, J. N. Davidson, and M. P. Foster, "Analysis, Design and Modelling of Two Fully-Integrated Transformers with Segmental Magnetic Shunt for LLC Resonant Converters," in *IECON 2020 The 46th Annual Conference of the IEEE Industrial Electronics Society*, 2020: IEEE, pp. 1273-1278.

[9] J. Biela and J. W. Kolar, "Analytic model inclusive transformer for resonant converters based on extended fundamental frequency analysis for resonant converter-design and optimization," *IEEE Transactions on Industry Applications*, vol. 126, no. 5, pp. 568-577, 2006.

- [10] Z. Fang, Z. Huang, H. Jing, and F. Liu, "Hybrid mode-hopping modulation for LLC resonant converter achieving high efficiency and linear behaviour," *IET Power Electronics*, vol. 13, no. 6, pp. 1153-1162, 2020.
- [11] W. Chen, P. Rong, and Z. Lu, "Snubberless bidirectional DC-DC converter with new CLLC resonant tank featuring minimized switching loss," *IEEE Transactions on industrial electronics*, vol. 57, no. 9, pp. 3075-3086, 2009.
- [12] Y. Wei, Q. Luo, and A. Mantooh, "Overview of modulation strategies for LLC resonant converter," *IEEE Transactions on Power Electronics*, vol. 35, no. 10, pp. 10423-10443, 2020.
- [13] C. W. Tsang, M. P. Foster, D. A. Stone, and D. T. Gladwin, "Analysis and design of LLC resonant converters with capacitor-diode clamp current limiting," *IEEE Transactions on Power Electronics*, vol. 30, no. 3, pp. 1345-1355, 2014.
- [14] J.-H. Jung, H.-S. Kim, M.-H. Ryu, and J.-W. Baek, "Design methodology of bidirectional CLLC resonant converter for high-frequency isolation of DC distribution systems," *IEEE Transactions on Power Electronics*, vol. 28, no. 4, pp. 1741-1755, 2012.
- [15] Z. U. Zahid, Z. M. Dalala, R. Chen, B. Chen, and J.-S. Lai, "Design of bidirectional DC-DC resonant converter for vehicle-to-grid (V2G) applications," *IEEE Transactions on Transportation Electrification*, vol. 1, no. 3, pp. 232-244, 2015.
- [16] J. Min and M. Ordonez, "Bidirectional resonant CLLC charger for wide battery voltage range: Asymmetric parameters methodology," *IEEE Transactions on Power Electronics*, vol. 36, no. 6, pp. 6662-6673, 2020.
- [17] S. A. Ansari, J. N. Davidson, M. P. Foster, and D. A. Stone, "Design and analysis of a Fully-integrated planar transformer for LCLC resonant converters," in *2021 23rd European Conference on Power Electronics and Applications (EPE'21 ECCE Europe)*, 2021: IEEE, pp. P. 1-P. 8.
- [18] Y. Liu, H. G. Wu, J. Zou, Y. Tai, and Z. Ge, "CLL Resonant Converter with Secondary Side Resonant Inductor and Integrated Magnetics," *IEEE Transactions on Power Electronics*, vol. 36, no. 10, pp. 11316 - 11325, 2021.
- [19] M. H. Ahmed, A. Nabih, F. C. Lee, and Q. Li, "Low-loss integrated inductor and transformer structure and application in regulated LLC converter for 48-V bus converter," *IEEE Journal of Emerging and Selected Topics in Power Electronics*, vol. 8, no. 1, pp. 589-600, 2019.
- [20] S. De Simone, C. Adragna, and C. Spini, "Design guideline for magnetic integration in LLC resonant converters," in *2008 International Symposium on Power Electronics, Electrical Drives, Automation and Motion*, 2008: IEEE, pp. 950-957.
- [21] B. Li, Q. Li, and F. C. Lee, "High-frequency PCB winding transformer with integrated inductors for a bi-directional resonant converter," *IEEE Transactions on Power Electronics*, vol. 34, no. 7, pp. 6123-6135, 2018.
- [22] S. A. Ansari, J. Davidson, and M. Foster, "Fully-integrated planar transformer with a segmental shunt for LLC resonant converters," *IEEE Transactions on Industrial Electronics*, vol. 69, no. 9, pp. 9145 - 9154, 2021.
- [23] S. A. Ansari, J. Davidson, and M. Foster, "Inserted-shunt Integrated Planar Transformer with Low Secondary Leakage Inductance for LLC Resonant Converters," *IEEE Transactions on Industrial Electronics*, vol. 70, no. 3, pp. 2652 - 2661, 2022.
- [24] J. Zhang, Z. Ouyang, M. C. Duffy, M. A. Andersen, and W. G. Hurley, "Leakage inductance calculation for planar transformers with a magnetic shunt," *IEEE Transactions on Industry Applications*, vol. 50, no. 6, pp. 4107-4112, 2014.
- [25] S. A. Ansari, J. N. Davidson, and M. P. Foster, "Fully-integrated transformer with asymmetric leakage inductances for a bidirectional resonant converter," in *11th International Conference on Power Electronics, Machines and Drives (PEMD 2022)*, 2022, vol. 2022: IET, pp. 260-265.
- [26] A. Taylor, J. Lu, L. Zhu, K. H. Bai, M. McAmmond, and A. Brown, "Comparison of SiC MOSFET-based and GaN HEMT-based high-efficiency high-power-density 7.2 kW EV battery chargers," *IET Power Electronics*, vol. 11, no. 11, pp. 1849-1857, 2018.
- [27] W. G. Hurley and W. H. Wölfle, *Transformers and inductors for power electronics: theory, design and applications*. John Wiley & Sons, 2013.
- [28] M. Li, Z. Ouyang, B. Zhao, and M. A. Andersen, "Analysis and modeling of integrated magnetics for LLC resonant converters," in *IECON 2017-43rd Annual Conference of the IEEE Industrial Electronics Society*, 2017: IEEE, pp. 834-839.
- [29] Z. Ouyang, J. Zhang, and W. G. Hurley, "Calculation of leakage inductance for high-frequency transformers," *IEEE Transactions on Power Electronics*, vol. 30, no. 10, pp. 5769-5775, 2014.
- [30] S. A. Ansari, J. N. Davidson, and M. P. Foster, "Fully-Integrated Solid Shunt Planar Transformer for LLC Resonant Converters," *IEEE Open Journal of Power Electronics*, vol. 3, pp. 26 - 35, 2021, doi: 10.1109/OJPEL.2021.3137016.
- [31] *Magnetics Ferrite Catalog*, Magnetics, 2013. [Online]. Available: www.mag-inc.com.
- [32] S. A. Ansari, J. N. Davidson, M. P. Foster, and D. A. Stone, "Analysis of Test Methods for Measurement of Leakage and Magnetising Inductances in Integrated Transformers," in *2022 24th European Conference on Power Electronics and Applications (EPE'22 ECCE Europe)*, 2022: IEEE, pp. 1-10.



Sajad A. Ansari was born in Shahrood, Iran, in 1994. He received the B.S. and M.S. degrees in electrical engineering from Shahrood University of Technology, Shahrood, Iran in 2016 and Amirkabir University of Technology, Tehran, Iran in 2019, respectively. He is currently pursuing his PhD in the Department of Electronic and Electrical Engineering at The University of Sheffield, Sheffield, UK. His research interests include renewable energy and design and control of power electronic converters.



Jonathan N. Davidson received the M.Eng. degree in electronic engineering and the Ph.D. degree in thermal modelling and management from the University of Sheffield, Sheffield, U.K., in 2010 and 2015, respectively. In 2015, he became a Lecturer in electrical engineering at the University of Sheffield. He was made Senior Lecturer in 2022. His research interests include thermal modelling and management of power electronics, and the design and analysis of piezoelectric transformer-based power converters, high-voltage power supplies for plasma chemistry and wastewater sensing systems.



Martin P. Foster received the B.Eng. degree in electronic and electrical engineering, the M.Sc.(Eng.) degree in control systems, and the Ph.D. degree for his thesis "Analysis and Design of High-order Resonant Power Converters" all the University of Sheffield, Sheffield, U.K., in 1998, 2000, and 2003, respectively. Since 2003, he has been a member of the academic staff in the Department of Electronic and Electrical Engineering, The University of Sheffield, where he is involved in power electronic systems. His current research interests include the modelling and control of switching power converters, resonant power supplies, multilevel converters, battery management, piezoelectric transformers, power electronic packaging, and autonomous aerospace vehicles.